1

# Reduced Order Multiscale Model for Compression Kink-Band Failure in Composites

Journal Title
XX(X):3–41

DOI: 10.1177/ToBeAssigned
www.sagepub.com/
SAGE

2 **Alex Faupel[1], Ido Meshi[2], and Caglar Oskay[1]**

*Prepared using* sagej.cls

**Abstract**

A multiscale model for compression kink band failure in fibrous composites is presented. The computational model predicts the progression of damage associated with the formation of kink bands, which experiments demonstrate to involve excessive shear straining of the matrix material and fiber fracture. The uniqueness of the study is establishing the concurrent treatment of nonlinear deformation and failure of the composite constituents at the scale of the material microstructure, and the formation of kink bands at the mesoscopic scale. The model incorporates computational homogenization of the material response, a nonlocal gradient regularization scheme, and a curvature-based criterion for macroscopic fiber break to predict kink band formation. The multiscale approach resolves mesoscale mechanisms associated with kink banding while offering computational benefits compared to direct mesomechanical approaches. An accessible implementation within finite element analysis software is presented and the model is verified with analysis of a mesoscale domain incorporating initial fiber waviness. In quasi-static simulations, the kink band initiates due to matrix softening that results in the onset of buckling and is completely formed when fibers break as a result of localized curvature. Results from parametric studies confirm that compression strength is not directly related to measures of the kink band morphology, but it is strongly correlated with the shear strength and initial fiber misalignment angle. The predicted effects of material properties representing various carbon fiber reinforced polymers and a range of fiber misalignment angles on kink band width and failure strength corroborate analytical and experimental results presented in the literature.

**Keywords**

Multiscale modeling, Reduced order modeling, Progressive damage analysis, Compression kink band failure, Gradient-based regularization

## Introduction

Among the mechanisms contributing to compression failure of composite materials is the formation of kink bands. The importance of kink band failure is observed in experiments, where the strength under compression in the longitudinal direction is significantly lower than under tension[1,2]. Therefore, it should be accounted for in the modeling and designing of composites under compression.

Foundational experiments reveal some key features of kink band failure. Soutis et al.[3] report that in both notched and unnotched laminated plates with varying layups the compressive failure is linked to inelastic microbuckling of the longitudinal plies. In Kyriakides et al.[4] and Vogler and Kyriakides[5] the importance of initial fiber misalignment (or "imperfection") amplitude on compressive strength is demonstrated. Moreover, it is observed that post-failure, deformation of the composite was localized into kink bands which formed at inclinations with respect to the longitudinal and transverse directions of the loading. The measurements for kink band width in carbon fiber reinforced plastics (CFRPs) are reported in the range of $5 - 40$ times the fiber diameter[4,6,7,9,10]. Moran et al.[10],[11] investigated the formation and

[1]Department of Civil and Environmental Engineering,
Vanderbilt University, Nashville, TN 37235, USA
[2]School of Mechanical Engineering,
Tel-Aviv University, Israel

**Corresponding author:**
Caglar Oskay, VU Station B#351831, 2301 Vanderbilt Place, Nashville, TN 37235.
Email: caglar.oskay@vanderbilt.edu

propagation of kink bands in more detail, and reported the process of band broadening as the kink band propagates in graphite-thermoplastic composites (e.g. PEEK matrix material). The experimental imaging illustrates the kink band failure process to include excessive shear straining of the matrix material near the imperfection zone, fiber buckling, and tensile failure of buckled fibers forming the boundary of the kink band.

Further understanding of kink band formation and propagation has been derived from theoretical models. The general history for compressive strength prediction traces from Rosen's model[12] that considers the elastic buckling of adjacent fibers in phase with one another, "microbuckling", instigating deformation of the matrix material in shear. Argon's model[13] incorporated the local maximum initial fiber misalignment angle along with the in-plane shear strength of the matrix to predict compressive strength. More closely considering fiber rotation, Budiansky[14] incorporated the effect of fiber tensile failure and Budiansky and Fleck[15] and Fleck et al.[16] improved upon these theories and presented an elastic-perfectly plastic model where the development of a physical kink band is linked to the nonlinear relationship between fiber longitudinal modulus, matrix shear strength, and fiber diameter.

The nonlinear analytical descriptions and sensitivities of the failure mechanism have been studied using mesomechanical approaches that resolve fiber and matrix materials and incorporate fiber waviness where the fiber orientation varies in a sinusoidal fashion along the composite longitudinal direction. Studies utilizing direct numerical simulations include Yerramalli and Waas[17] where the positive effect of fiber diameter - and thus bending stiffness, on the compressive strength is confirmed using a 3D finite element simulation of a small cylindrical section of composite material comprised of purely elastic fibers and $J_2$ theory of plasticity matrix behavior. Bishara et al.[18] performed analyses with a single 3D row of composite material modeled as linear elastic

fibers that fail under normal tensile strain and an elastic-plastic matrix with isotropic hardening. Naya et al.[19] also directly simulate fibers surrounded by a plastically behaving matrix but arranged according to a statistical distribution in a column-like domain and modeled with a commercial continuum damage code, additionally including cohesive-frictional interfaces between the fibers and matrix. The contributions of the microstructure and initial fiber misalignment angle to the kink band process are simulated in detail, however parametric studies are carried out using a simplified single fiber model to obtain compression strength and elastic modulus. Other simulation results link the experimentally observed stages of the kink band process to matrix yielding in areas of imperfection and indicate the effect of initial fiber waviness locality on compressive strength. Bergan et al.[20] present a model connecting fiber rotation with mesoscopic compression failure by incorporating kink band width predicted from a micromechanical simulation as an input parameter. This model requires numerical schemes such as element deletion to obtain a load drop indicative of material failure and accurately captures kink band kinematics.

Criterion-based compression failure models that are influenced by or account for kink banding have also been proposed. In Pinho et al.[21], where kink band failure in the ply occurs according to a bound of the longitudinal composite strength and geometry-dependent calculations of in-situ shear strengths. Camanho et al.[22] presented an invariant-based criterion in the frame of localized fiber waviness which claims local transverse failure of the matrix as compression kink band failure. Alternatively, Wilhelmsson et al.[23] predicted failure of the composite material in shear due to maximum "defect severity" utilizing observations in an experimental database. While criterion-based models idealize the consequences of kink bands in predicting failure at the macroscale, these models do not resolve the mesoscale mechanisms associated with kink banding.

In this manuscript, we present a multiscale computational model for compression kink band formation in unidirectionally reinforced (UD) composites. The uniqueness of the study is establishing the concurrent treatment of nonlinear deformation and failure of the composite constituents at the scale of the material microstructure, and the formation of kink bands at the mesoscopic scale. This approach attempts to computationally bridge the primary mechanisms of matrix damage and fiber fracture and the consequent instability. The model incorporates computational homogenization of the material response and a nonlocal gradient regularization scheme to predict kink band formation. Verification of the model is undertaken with a mesoscale domain, where the effects of the initial fiber waviness and matrix material behavior are examined. Results from parametric studies correlate the composite material properties to compressive strength, and the relationships match theoretical investigations. By directly incorporating microstructural features and mesoscopic fiber waviness we link the microscopic state and provide physical context to compressive failure.

## Multiscale Compression Kink Band Model

The multiscale nature of failure in long fiber composite materials by compression kink banding is depicted in Fig. 1. Material properties and morphological features at several length scales affect the nucleation and propagation characteristics of compression kink bands. Among them, fiber waviness has a pronounced effect on the overall compression strength of the lamina as analyzed by Fleck et al.[16], Vogler et al.[24] and others. The wavelengths associated with fiber waviness observed in CFRPs are in the range of 70-800 times the fiber diameter in the composite[4,25]. The kink band itself, where fiber and matrix cracking, debonding, and severe matrix deformation coexist, is generally restricted to a width of no greater than a few hundred $\mu$m (mesoscale)[5,15]. The kink band width is sensitive to the

fiber diameter, which is approximately 5-10 $\mu$m - an order of magnitude smaller than the kink band width (microscale). On the other hand, the size of the structural component or specimen is several orders of magnitude larger than the kink band width (macroscale).

The significant disparity between the scales involved in the kink band induced failure allows the applicability of scale-separable multiscaling principles to this problem (e.g., computational homogenization[26,27]). The proposed modeling approach is a nonlocal generalization of the Eigenstrain-based reduced order computational homogenization modeling (EHM)[27–29]. In the remainder of this section, we provide an overview of "local" EHM, and generalize it to a nonlocal formulation. The specific features of the nonlocal compression kink-band model are then discussed.

### *Eigenstrain-based homogenization model (EHM)*

EHM is a multiscale progressive damage analysis approach for predicting the failure response of composites and other heterogeneous materials[30–33]. The basis of the formulation is the computational homogenization theory[34,35] coupled with transformation field analysis[36]. In EHM, certain information on the material microstructure such as localization operators, polarization tensors, influence functions and coefficient tensors[28] are computed by solving linear elastic microscale problems defined over the material unit cell or representative volume prior to the multiscale progressive damage and failure analysis of a composite structure. The microstructural information is bridged to the macroscopic scale through a reduced order microscale model. The nonlinear analysis and history dependent reduced order microstructure problem is tightly coupled with the structural scale analysis, which are concurrently evaluated (a separate reduced order model is evaluated and tracked at each quadrature point of the macroscale discretization). The precomputed coefficient tensors along with internal state variables are employed to homogenize or localize the

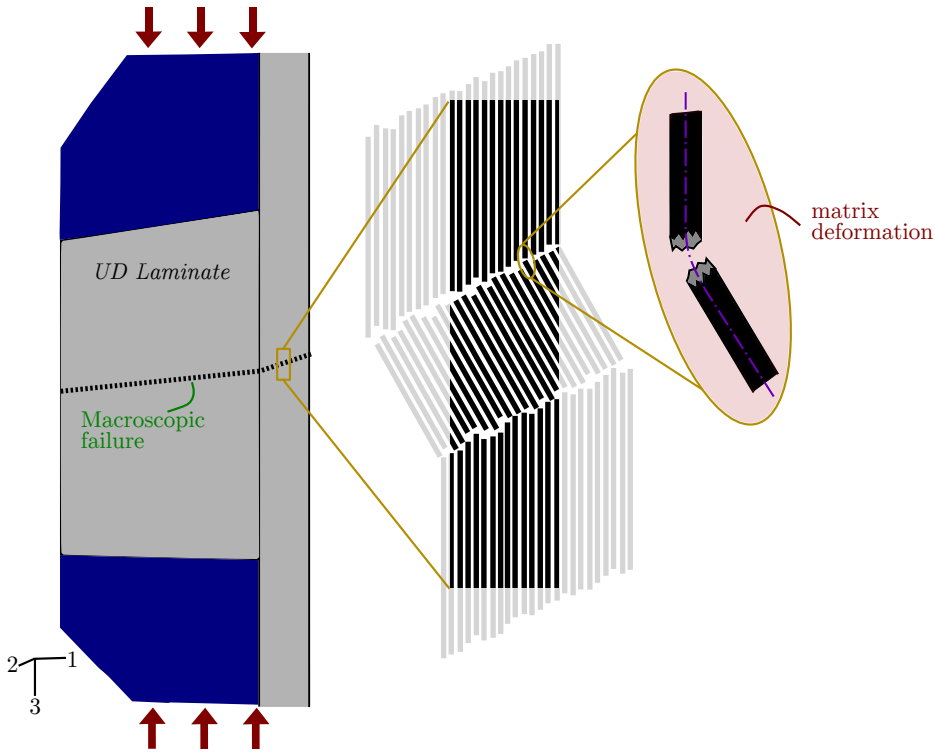


**Figure 1.** Observations of macroscopic compression failure in UD specimens include kink band formation that is linked to significant deformation and fiber curvature. (see e.g.,[7–9])

stress and strain fields. The reader is referred to Refs.[28,31] for details of the EHM formulation. The static force equilibrium at the macroscopic scale is expressed as:

$$\nabla \cdot \bar{\boldsymbol{\sigma}}(\mathbf{x}, t) = 0; \quad \mathbf{x} \in \mathcal{O}; \quad t \in [0, t_0] \tag{1}$$

where, $\bar{\boldsymbol{\sigma}}$ denotes the macroscopic (i.e., homogenized) Cauchy stress; $\mathbf{x}(\mathbf{X}, t) \in \mathcal{O}(t)$ is the position vector that parameterizes the current configuration of the macroscopic domain, $\mathcal{O}$, with the macroscopic reference (i.e., material) coordinates, $\mathbf{X}$, as illustrated in Fig. 2. We consider the evolution of the current configuration since kink band

formation is driven by macroscopic instability, and a large-deformation formulation at macroscale is necessary to capture the instability. The macroscopic boundary conditions are expressed as

$$\bar{\mathbf{u}} = \hat{\mathbf{u}}(\mathbf{X}, t);\ \mathbf{X} \in \Gamma_u^0 \tag{2}$$

$$\bar{\mathbf{P}} \cdot \mathbf{N} = \hat{\mathbf{t}}(\mathbf{X}, t);\ \mathbf{X} \in \Gamma_t^0 \tag{3}$$

in which, $\bar{\mathbf{u}}(\mathbf{X}, t)$ denotes the macroscopic displacement field; $\hat{\mathbf{t}}(\mathbf{X}, t)$ and $\hat{\mathbf{u}}(\mathbf{X}, t)$ are respectively the prescribed tractions and displacements applied on boundaries $\Gamma_t^0$ and $\Gamma_u^0$ of the undeformed configuration, $\mathcal{O}^0 := \mathcal{O}(0)$; $\mathbf{N}$ is the unit outward normal to $\Gamma_t$; and $\bar{\mathbf{P}}$ is the macroscopic first Piola-Kirchoff stress. Considering the macroscopic deformation gradient, $\bar{\mathbf{F}} = \partial\bar{\mathbf{u}}/\partial\mathbf{X} - \boldsymbol{\delta}$ (with $\boldsymbol{\delta}$ the second order identity tensor), we employ the logarithmic measure to track macroscopic strain, $\bar{\boldsymbol{\epsilon}}$:

$$\bar{\boldsymbol{\epsilon}} = \ln \bar{\boldsymbol{V}} \tag{4}$$

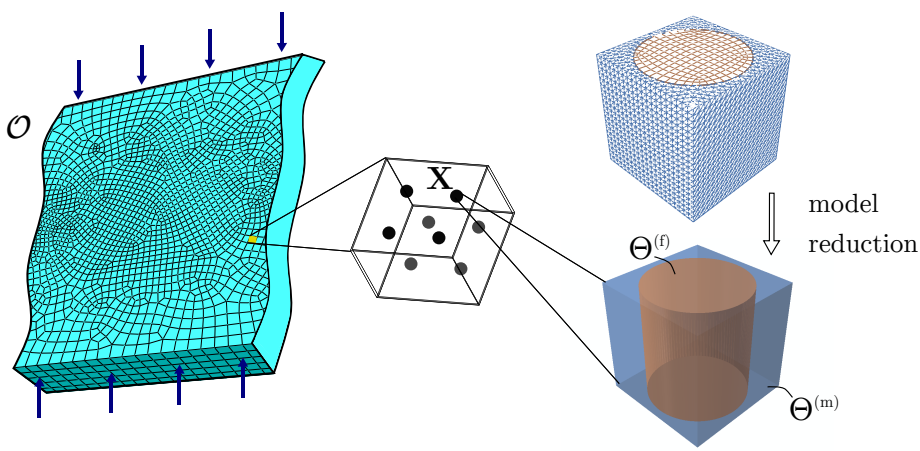


**Figure 2.** The multiscale modeling approach using EHM for fiber kinking employs a reduced-order microstructural response.

where, $\bar{\boldsymbol{V}} = \sqrt{\bar{\mathbf{F}}\bar{\mathbf{F}}^T}$ is the left stretch tensor. Considering the brittle characteristics of the constituents of the composite, the large deformations observed in the composite specimen are due to large rotations coupled with small microscopic distortions up to the onset of failure. A local coordinate system is attached to the microstructure that rotates with the macroscopic rotation such that the microstructural stresses are not affected by the rigid body motion of the microstructure (i.e., the co-rotational frame is used). Progressive damage accumulation that leads to macroscopic instability and failure is modeled using continuum damage mechanics approach. The constitutive response of the composite constituents (i.e., fiber and matrix) is described by damage variables. By this representation and microstructural model order reduction through EHM, the Cauchy stress, $\hat{\bar{\boldsymbol{\sigma}}}$, in the co-rotational frame is expressed as:

$$\hat{\bar{\boldsymbol{\sigma}}} = \sum_{\Delta=1}^{n} \left\{ \left[1 - \omega^{(\Delta)}\right] \left[ \bar{\mathbf{L}}^{(\Delta)} : \hat{\bar{\boldsymbol{\epsilon}}} + \sum_{\alpha=1}^{n} \bar{\mathbf{P}}^{(\alpha\Delta)} : \boldsymbol{\mu}^{(\alpha)} \right] \right\} \tag{5}$$

in which $\hat{\bar{\boldsymbol{\epsilon}}}$ is macroscopic strain rotated to the co-rotational frame, $\omega^{(\Delta)}$ denotes a part-average damage variable associated with a subdomain (or part) of microstructure $\Theta^{(\Delta)} \subset \Theta$ ($\Theta$ denotes the domain of the microstructure) and taken to be constant within $\Theta^{(\Delta)}$; $\boldsymbol{\mu}^{(\Delta)}$ is the part-average inelastic strain field induced by the damage in the microstructure subdomain, $\Delta$; $\bar{\mathbf{L}}^{(\Delta)}$ and $\bar{\mathbf{P}}^{(\alpha\Delta)}$ are coefficient tensors computed using the influence functions and elastic properties of the constituents. The partitioning of the material morphology into subdomains and the spatially piece-wise constant approximation for damage and damage-induced inelastic strain fields constitute the order reduction strategy. While Fig. 2 illustrates partitioning of the microstructure into the matrix and fiber phases, other partitioning strategies are also possible as explored in[25,29]. The kinematic equation that relates the inelastic strain coefficients to the

178 macroscopic strain is expressed as:

$$\sum_{\Delta=1}^{n}\left\{\left[1-\omega^{(\Delta)}\right]\left[\hat{\mathbf{A}}^{(\alpha\Delta)}:\bar{\boldsymbol{\epsilon}}+\sum_{\gamma=1}^{n}\hat{\mathbf{B}}^{(\alpha\Delta\gamma)}:\boldsymbol{\mu}^{(\gamma)}\right]\right\}=0,\quad\forall\alpha=1,...,n \tag{6}$$

179 in which $\hat{\mathbf{A}}^{(\alpha\Delta)}$ and $\hat{\mathbf{B}}^{(\alpha\Delta\gamma)}$ are additional coefficient tensors. This system
180 of equations for the reduced order model is closed by defining evolution
181 equations of the part-average damage variable, $\omega^{(\Delta)}$, which is driven
182 by the local damage history variable, $\kappa^{(\Delta)}$. At a fixed, but arbitrary
183 macroscopic material point:

$$\omega^{(\Delta)}=\Phi(\kappa^{(\Delta)});\;\;0\leq\Phi\leq1 \tag{7}$$

184 The scalar damage variable $0\leq\omega^{(\Delta)}<1$ indicates the current damage
185 state of the composite constituent occupying $\Theta^{(\Delta)}$; the limits $\omega^{(\Delta)}=0$
186 and $\omega^{(\Delta)}\rightarrow1$ respectively indicate no damage and complete loss of load
187 carrying capacity within the subdomain of the microstructure. The part
188 damage variable evolves according to the monotonic damage evolution
189 function:

$$\Phi(\kappa^{(\Delta)})=\frac{\arctan\left(a^{(\Delta)}\langle\kappa^{(\Delta)}-\kappa_0^{(\Delta)}\rangle-b^{(\Delta)}\right)+b^{(\Delta)}}{\frac{\pi}{2}+\arctan\left(b^{(\Delta)}\right)} \tag{8}$$

190 in which $a^{(\Delta)}$, $b^{(\Delta)}$, ${\kappa_0}^{(\Delta)}$ are the material parameters that define the
191 failure behavior of the composite constituent occupying $\Theta^{(\Delta)}$ (i.e., matrix
192 or fiber), and the Macaulay brackets, $\langle\cdot\rangle$, enforce the threshold for the
193 onset of inelastic evolution of damage. The part damage history variable
194 is computed as:

$$\kappa^{(\Delta)}=\max_{0\leq\tau\leq t}\{\upsilon^{(\Delta)}(\mathbf{X},\tau)\} \tag{9}$$

taking the value of the maximum damage equivalent strain, $\upsilon^{(\Delta)}$, in the loading history. The damage equivalent strain is defined as:

$$\upsilon^{(\Delta)} = \sqrt{\frac{1}{2}\hat{\boldsymbol{\epsilon}}^{(\Delta)} : \widehat{\mathbf{L}}^{(\Delta)} : \hat{\boldsymbol{\epsilon}}^{(\Delta)}} \tag{10}$$

which is a function of the local principal strains, $\hat{\epsilon}^{(\Delta)}$, and the elastic modulus tensor, $\widehat{\mathbf{L}}^{(\mathbf{\Delta})}$, rotated to the principal directions. The evolution equations that drive the progressive failure of the composite constituents defined in Eqns. (7)-(10) are macroscopically local in character. This means that the damage evolution within subdomain $\Theta^{(\Delta)}$ at a macroscopic material point is driven by the state of strain and the damage history variable of that macroscopic material point alone. As further explained below, we propose a nonlocal generalization of this approach to better control the thickness of the compression kink band.

*EHM model for fiber kinking* The EHM model as employed to idealize compression kink banding is illustrated in Fig. 2. Experimental investigations demonstrate a number of failure processes that either contribute to or result from compression kink bands, including nonlinear shear deformation and damage in the matrix concentrated in the kink band region, fiber fracture (particularly along the edges of the kink band) and fiber-matrix debonding[7]. The microstructure is idealized as a periodic and square unit cell. In view of the fact that the kink band zone exhibiting significant matrix deformation and failure is much larger than the size of the unit cell, we employ an EHM model that consists of 2 parts (i.e., $n = 2$) and considers uniform damage accumulation in the matrix and fiber subdomains of the unit cell. It is also possible to incorporate the progressive debonding mechanism[27,37], along the fiber-matrix interface, but we exclude this effect to retain simplicity of the model. It is noteworthy that a majority of prior investigations considered elastic-plastic (see e.g.[16]) or elastic-viscoplastic ([24]) matrix behavior in

direct numerical simulation of compression failure. The current study employs a continuum damage model that exhibits a nonlinear hardening behavior followed by material softening. While plasticity was shown to be sufficient to model kink bands, we contend that the relatively brittle matrix response (even considering nonlinear shear effects) could be better captured by a model that incorporates matrix failure.

### *Gradient-based regularization*

Initiating from a region of high fiber waviness, localized buckling of the fibers promoted by nonlinear deformation of the matrix yields a kink band region that is many fiber diameters wide[15]. This region is marked by significant fiber rotations, reduced stress carrying capacity, and shear deformation in the matrix. Early analytical studies in[16,24] have shown that the width of the kink band is strongly affected by fiber diameter, which controls fiber bending rigidity. This effect has been also studied using direct numerical simulations[17]. EHM and other first order homogenization methods cannot directly account for fiber bending at the microscale. While higher order homogenization[38,39] formulations could capture this effect, several computational complications have so far limited their use. Instead, we propose a nonlocal extension of the EHM model to control kink band width in multiscale simulations. Let $\omega^{(\mathrm{m})}(\mathbf{x}, t)$ denote the damage state of the matrix subdomain of the unit cell associated with a fixed but arbitrary position on the current configuration, $\mathbf{x}$ at time $t$. The damage variable is re-written as a function of a *nonlocal* equivalent damage variable, $\bar{\kappa}^{(m)}(\mathbf{x}, t)$ as:

$$\omega^{(\mathrm{m})} = \Phi(\bar{\kappa}^{(\mathrm{m})}); \;\; 0 \leq \Phi \leq 1 \tag{11}$$

In contrast with $\kappa^{(\mathrm{m})}$ in Eqn. 7, which is a local history variable, $\bar{\kappa}^{(\mathrm{m})}$ is a field variable, the spatial variation of which is governed by the following

expression:

$$\bar{\kappa}^{(\mathrm{m})}(\mathbf{x},t) - {L_0}^2\nabla^2\left[\bar{\kappa}^{(\mathrm{m})}(\mathbf{x},t)\right] = \hat{\kappa}^{(\mathrm{m})}(\mathbf{x},t); \tag{12}$$

in which $L_0$ is a length scale parameter, and $\nabla^2$ denotes the Laplacian operator. $\hat{\kappa}^{(\mathrm{m})}$ is defined as:

$$\hat{\kappa}^{(\mathrm{m})}(\mathbf{x},t) = \min\{\kappa^{(\mathrm{m})}, \kappa_c\} \tag{13}$$

where $\kappa_c$ denotes the value of the local history variable when full damage is reached (i.e., $\Phi(\kappa = \kappa_c) = 1$). Since $\Phi$ defined in Eqn. 8 only asymptotes to unity, a value slightly less than unity is used to define $\kappa_c$ (i.e., $\Phi(\kappa_c) = 1 - \epsilon$) in the numerical implementation. Neumann boundary conditions are enforced to evaluate the nonlocal equation:

$$\nabla\bar{\kappa}^{(\mathrm{m})} \cdot \mathbf{n} = \mathbf{0} \tag{14}$$

where $\mathbf{n}$ is the unit outward normal to the domain boundaries.

The numerical evaluation of the proposed nonlocal EHM model solves for two cardinal unknown variables at the macroscopic scale, which are the macroscopic displacements, $\bar{\mathbf{u}}$, and the nonlocal damage history field, $\bar{\kappa}$. The primary idea behind the use of the nonlocal equation is to spatially distribute the effect of $\kappa^{(\mathrm{m})}$ localized at a position coordinate, $\boldsymbol{x}$, to a neighborhood around $\boldsymbol{x}$. The size of this neighborhood is dictated by the length scale parameter, $L_0$, which is therefore directly correlated with, but not necessarily equal to, the kink band width. The dissipative effect of the nonlocal equation is illustrated in Fig. 3. The figure illustrates the analytical solution of the one-dimensional version of Eqn. 12 ($u(x) - L_0^2 d^2u(x)/dx^2 = \delta(x)$), for which the right hand side (i.e., local variable) is set to the Dirac delta distribution centered at $x = 0$. The figure illustrates how the source (i.e., right hand side) is spatially smoothened out with increasing value of the length scale parameter.

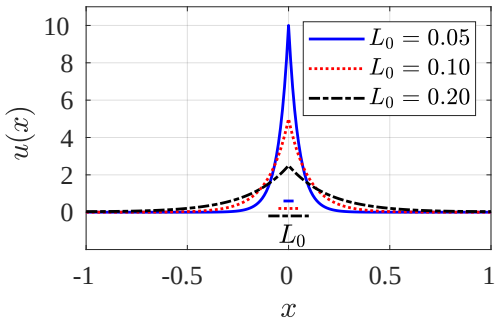


**Figure 3.** The effect of the length scale parameter on the unknown field, $u(x)$, for 3 values of $L_0$.

In order to give a physical meaning to the length scale parameter, $L_0$, we turn to the work of Fleck et al.[16]. For a kink band with a kink band angle, $\beta = 0$, Fleck et al.[16] analytically computed the band width as:

$$\frac{w}{d} = \frac{\pi}{4}\left(\frac{E}{2\tau_Y}\right)^{\frac{1}{3}} \tag{15}$$

where $d$ denotes the fiber diameter, $E$ is the modulus of the composite along the fiber direction, and $\tau_y$ is the composite shear strength. Our numerical simulations described below suggest a linear relationship between the length scale parameter in the nonlocal equation and the kink band width as follows:

$$L_0 = aw + b = \frac{ad\pi}{4}\left(\frac{E}{2\tau_Y}\right)^{\frac{1}{3}} + b \tag{16}$$

where, $a$ and $b$ are model parameters, the calibration of which is presented below. Extension of the analytical expression of kink band width with non-zero band angles is provided in Refs.[6,15]. A relationship could be obtained for the aforementioned and other analytical relationships in a similar way.

After the onset of full damage in the matrix (i.e., $\omega^{(\mathrm{m})} \approx 1$) and consequently the kink band formation, the value of the local history variable, which is a measure of local deformation, could increase substantially in the band. This results in a very large local source term in the nonlocal equation and leads to convergence issues in its numerical evaluation. In order to alleviate these issues, the source term is not allowed to increase beyond the critical value, $\kappa_c$ as indicated by Eqn. 13.

The classical nonlocal damage formulations with gradient type regularization are known to exhibit an expansion of the damage region even after complete failure is observed[40]. Under tensile loading, growth of the damage region is spurious. In the current compression case, this effect results in a steady state broadening of the kink band after the onset of instability. Interestingly, experimental observations do point to a physical band broadening phenomena as observed in Refs.[5,10,11]. However the experimental observations refer to an increase of kink band width of a propagating band, and at a fixed spatial position does not grow. We adopt a technique presented by Poh et al.[40] to control the growth of the kink band after it is formed. It is expected that fully damaged matrix material no longer carries load, and the nonlocal influence of a critically damaged material point on its neighborhood should diminish. Spread of the kink band is controlled by dynamically setting the length scale parameter to reduce as matrix damage evolves (referred herein as the Variable Length Scale formulation or VLS).

$$L(\mathbf{x}, t) = g\left(\omega^{(\mathrm{m})}(\mathbf{x}, t)\right) L_0 \tag{17}$$

$$g = \sqrt{\frac{(1-R)\exp\left(-\eta\omega^{(\mathrm{m})}\right) + R - \exp\left(-\eta\right)}{1 - \exp\left(-\eta\right)}} \tag{18}$$

where, $R$ and $\eta$ are numerical constants that control the evolution of the length scale parameter as a function of matrix damage. The constant $L_0$

in Eqn. 12 is replaced by $L$. Figure 4 illustrates the variation of the length scale parameter as a function of the history and damage variables. The length scale parameter decreases sharply only when the damage parameter becomes close to unity, whereas it is approximately constant for low states of damage.

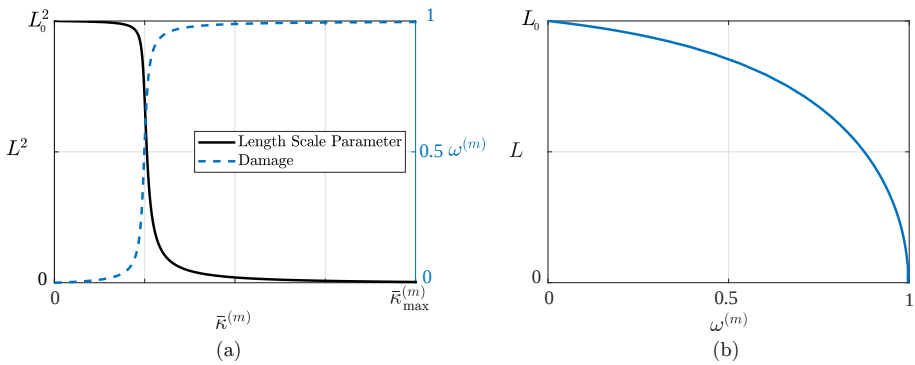


**Figure 4.** (a) Degradation of the length scale parameter and accumulation of damage; (b) relationship between the length scale parameter and damage.

## *Fiber Breakage*

Fibers in the kink band region undergo bending and ultimately break in tension during unstable localized buckling. In this study, we propose a simple curvature-based criterion to describe fiber break at the macroscopic scale. Let $\theta^{'}(\mathbf{x}, t)$ denote the orientation of the fiber at the reference macroscopic coordinate, $\mathbf{x}$.

Fiber curvature is then described as $\rho = d\theta^{'}/dz$, where $z$ is the direction along the fiber. The fiber damage model is described as follows:

$$\omega^{(f)} = \begin{cases} 0 \text{ if } \rho < \rho_{crit} \\ 1 \text{ if } \rho \geq \rho_{crit} \end{cases} \tag{19}$$

where, $\rho_{crit}$ is a critical curvature value.

It is important to note that the curvature is also a nonlocal value as it requires the spatial gradient of fiber orientation. Details of the computational implementation is discussed below.

### *Numerical implementation*

The nonlocal damage formulation presented above was implemented along with the EHM model to predict the compression failure behavior of a unidirectional composite. The model solves the additional partial differential equation (Eq. (12)) for the nonlocal equivalent damage scalar variable, $\overline{\kappa}$, fully coupled with the macroscopic stress equilibrium problem (Eq. (1)). Conveniently, this coupled system of equations is analogous to that of a coupled thermo-mechanical problem since Eq. (12) can be recast in the form of the steady-state heat equation with a temperature-dependent and nonlinear source term: $r$.

$$\nabla^2 \left[ L^2 \bar{\kappa}(\mathbf{x}, t) \right] = r(\mathbf{x}, t) \tag{20}$$

where, $r$ denotes the source term, which is a function of the damage history variable.

$$r(\mathbf{x}, t) = \hat{\kappa}(\mathbf{x}, t) - \bar{\kappa}(\mathbf{x}, t) \tag{21}$$

By leveraging this form for the nonlocal equation, the multiscale reduced order system was implemented in the commercial finite-element software Abaqus. The proposed implementation algorithm is adapted from the work of Seupel et al.[41] and summarized in Fig. 5. Given the unit cell geometry and 2-part reduced order model partitioning shown in Fig. 2, the coefficient tensors are computed at the preprocessing stage (see Crouch and Oskay[27] for details of coefficient tensor computations). The coefficient tensors along with the model parameters that describe damage evolution within the composite constituents are inputs to the multiscale nonlocal reduced order system. The multiscale system is

evaluated by the thermomechanical analysis capability in Abaqus, which solves the macroscale equilibrium and the nonlocal equations in a tightly coupled manner. The evolution of the reduced order microscale problem is treated as stress update and implemented using the user supplied material behavior capability (UMAT). This incremental-iterative update procedure returns the macroscopic Cauchy stress, the tangent stiffness, and the local history variable. The local history variable $\hat{\kappa}$, which forms part of the source term of the nonlocal equation, is passed to the HETVAL subroutine, where the total source term, $r$, is calculated and returned along with the gradient terms for Jacobian computation. Incremental evaluation

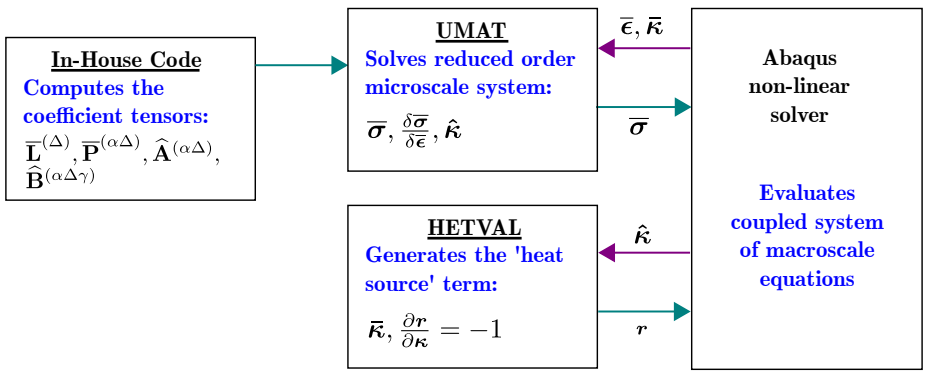


**Figure 5.** Computational procedure for nonlocal damage model.

by the nonlinear solver updates the displacement and nonlocal history variable (i.e., temperature) fields. To complete the thermal analogy, the nonlocal variable changes in the case that the heat source solution is nonzero. The ”conductivity” of the material (according to the thermal analogy) corresponds to the length scale parameter. The VLS model, where a solution dependent length scale parameter is considered, is implemented by tabulating the temperature-dependent isotropic thermal conductivity property of the material definition (tabulating $L$ dependency on $\bar{\kappa}$ according to Eqn. 17). An alternate form to tabular data entry is

the use of user supplied material behavior for the thermal problem (using UMATHT).

*Fiber Break Routine* Fiber break is incorporated as an online procedure in the user supplied subroutine by updating global variable arrays of the material point orientations during the simulation. For each element of the macroscopic discretization, the neighboring elements along the fiber direction, and distances to neighboring element centroids are calculated at the beginning of the analysis. The orientation of an element centroid during an increment is calculated as the average of the orientations at the material points belonging to that element. The orientation values are extracted by performing polar decomposition on the current deformation gradient in the local frame (a tutorial for obtaining the relevant information from Abaqus is provided by[42]). The curvature is approximated using a first order finite difference scheme based on the element-wise information at the end of every increment. The primary equations implemented in this routine are as follows:

$$\rho(\tilde{\mathbf{x}}, t) = \left| \frac{\theta^{'}(\tilde{\mathbf{x}}, t) - \theta^{'}(\tilde{\mathbf{x}}^{\text{neighbor}}, t)}{z(\tilde{\mathbf{x}}, 0) - z(\tilde{\mathbf{x}}^{\text{neighbor}}, 0)} \right| \tag{22}$$

$$\theta^{'}(\tilde{\mathbf{x}}, t) = \cos^{-1}\left( \frac{tr(\mathbf{R}(\tilde{\mathbf{x}}, t)) - 1}{2} \right) \tag{23}$$

$$\bar{\mathbf{F}} = \bar{\mathbf{V}} \cdot \mathbf{R} \tag{24}$$

$\theta^{'}$ is a calculation for absolute orientation relative to the initial configuration (see e.g.,[43]), and the definition for $z$ is the same as in the section, *Fiber Breakage*. The neighboring centroid position with respect to an element centroid $\tilde{\mathbf{x}}$ is denoted $\tilde{\mathbf{x}}^{\text{neighbor}}$. $\mathbf{R}$ is the rotation matrix which relates the orientation of the current configuration to the initial local frame. $\bar{\mathbf{F}}$ and $\bar{\mathbf{V}}$ are the deformation gradient and the left stretch tensor in the current configuration as defined in the section, *Eigenstrain-based*

376 *homogenization model*. Once critical curvature is reached for an element,
377 the fiber stiffness is set to zero, i.e. $\omega^{(\mathrm{f})} = 1$.

## 378 Mesoscale Investigations

### 379 Problem setup

380 Verification of the proposed multiscale model for modeling kink band
381 formation is performed using a mesoscale configuration of a uni-
382 directional composite shown in Fig. 6. The mesostructure is subjected
383 to displacement-controlled loading at one end along the z-direction. The
384 lateral faces of the structure are assigned periodic boundary conditions.
385 The geometry and boundary conditions allow the investigations to focus
386 particularly on the onset of kink banding (i.e., initiation). The dimensions
387 of the mesostructure domain are indicated in Fig. 6. Analyses are
388 undertaken with the discretized column geometry made of C3D8T linear
389 hexahedral solid elements. The solution proceeds with automatic time
390 stepping and constant stabilization throughout the loading. Both force
391 and heat flux equilibrium states are solved at the macroscopic domain
392 according to the coupled thermo-mechanical analysis scheme described
393 in Section 2.3.

394 The unit cell idealizing the microstructure of a generic graphite
395 fiber/toughened epoxy material system shown in Fig. 2 with a 65 percent
396 fiber volume fraction is employed to construct the EHM model. The elastic
397 properties of the transversely isotropic fiber and the elastic and damage
398 properties of the isotropic matrix are adopted from Ref.[31] and summarized
399 in Table 1. The fibers are taken to behave elastically unless broken. The
400 damage evolution parameters were set in such a way that the resulting
401 composite properties under shear and tensile loading are in reasonable
402 agreement with the corresponding strengths reported from v-notch shear
403 and three-point bend tests outlined in Clay and Knoth[1]. $\kappa_0^{(\mathrm{m})}$ is selected
404 to be zero so that damage evolution occurs for $\bar{\kappa}^{(\mathrm{m})} > 0$. The remaining

parameters, $\eta$ and $R$, are numerical constants and the values were set to control the nonlocal damage effect and result in the relationships shown in Fig. 4.

**Table 1.** Elastic and damage parameters of the material constituents

| Elastic Parameters | | | Damage Parameters | | |
|---|---|---|---|---|---|
| Parameter | Unit | Value | Parameter | Unit | Value |
| $E_1^{(f)}$ | GPa | 12.45 | $a^{(\mathrm{m})}$ | $\mathrm{MPa}^{-1/2}$ | 1.5 |
| $E_3^{(f)}$ | GPa | 257.4 | $b^{(\mathrm{m})}$ | N/A | 2.5 |
| $G_{13}^{(f)}$ | GPa | 146.0 | $\kappa_0^{(\mathrm{m})}$ | $\sqrt{\mathrm{MPa}}$ | 0.0 |
| $\nu_{12}^{(f)}$ | N/A | 0.291 | $\eta$ | N/A | -2 |
| $\nu_{31}^{(f)}$ | N/A | 0.206 | R | N/A | -0.006 |
| $E^{(\mathrm{m})}$ | GPa | 3.70 | | | |
| $\nu^{(\mathrm{m})}$ | N/A | 0.377 | | | |

In order to introduce fiber waviness, a general fiber misalignment angle expression based on the material coordinate in the fiber layup direction is used. The element orientation function, $\psi$, is expressed in a trigonometric form similar to that found in other kink band analyses [18,24]:

$$\psi\left(x,y,z\right)=\tan^{-1}\left(\tan(\psi_0)\sin\left(\frac{\pi z}{l}\right)\right) \tag{25}$$

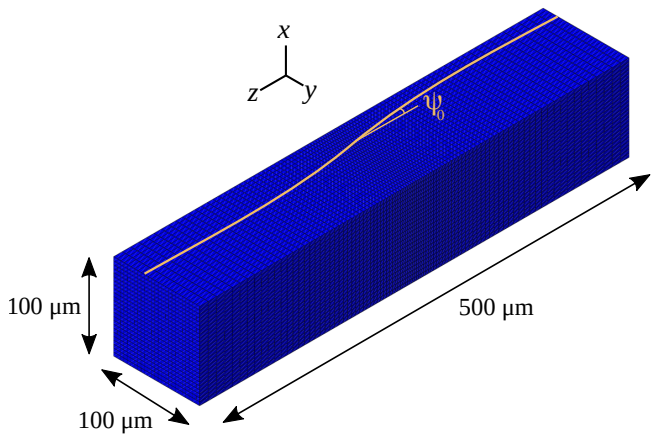


**Figure 6.** Mesoscale problem domain configuration (the gold line is a schematic of the fiber orientation).

where $z$ is the material coordinate in the fiber direction and $l$ is the half-wavelength of the function ($l = 0.5\,\mathrm{mm}$ in this example). The *misalignment angle* stated in this work refers specifically to the maximum initial misalignment angle $\psi_0$, which is prescribed at mid-height of the specimen. The local material orientation at each quadrature point in the initial frame is perturbed by the angle determined in Eq. 25 and introduced using the user subroutine, ORIENT, in Abaqus, where we supply the array of direction cosines for the desired material directions with respect to the global coordinate system.

### *Mesh sensitivity analysis*

In this section, we investigate the mesh size sensitivity of the regularized and unregularized EHM formulations for capturing kink band initiation. The unregularized formulation refers to the evaluation where damage evolution is driven by the local history variable and the nonlocal equation is not included in the implementation. The mesoscale sample is discretized using three different mesh densities. For efficiency, mesh refinements are considered particularly at mid-height, where the highest misalignment and hence the kink band is expected to originate. The coarse mesh has uniform element lengths of $10\,\mu\mathrm{m}$ from end-to-end and the fine mesh has element lengths tapering from $10\,\mu\mathrm{m}$ at the ends to $3\,\mu\mathrm{m}$ across the entire middle $150\,\mu\mathrm{m}$ long section of the domain. The maximum misalignment angle, $\psi_0$, is set to $2^\circ$.

Figure 7a shows the damage contours at the onset of kink band formation as predicted by the unregularized formulation using the fine and coarse meshes. The contours indicate that the predicted kink band width is dependent on the mesh size (a single layer of elements fails). Fiber break occurs at the failed element which forms the kink band with both meshes. The stress-strain behavior is shown in Fig. 8a and is identical between meshes. Introducing gradient-based regularization to capture nonlocal

damage in the material results in a thicker kink band as shown in Fig. 7b-c. Fiber breaks occur simultaneously in two equal thickness regions to form the kink band. The coarse mesh and fine mesh simulations predict the kink band width $w \approx 80\,\mu\mathrm{m}$ (or 10 times the fiber diameter), with a $1\,\mu\mathrm{m}$ difference due to the resolution limitation of the coarse mesh (width predictions can be made in multiples of element size). The stress-strain behavior predicted using the regularized model is nearly identical for both meshes as shown in Fig. 8b.

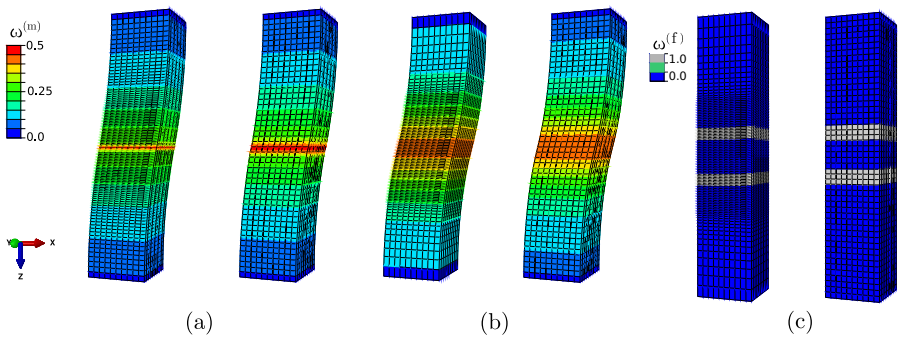


**Figure 7.** Sensitivity of damage development to mesh size with the (a) local and (b) nonlocal damage model formulation ($L_0 = 31.7\ \mu m$); (c) sensitivity of fiber-break prediction to mesh size (nonlocal damage model).

## *Kink Band Morphology*

*Kink Band Width Control* A parametric study is undertaken to investigate the effect of the length scale parameter on controlling the width of the kink band. As explained in the section, *Fiber Breakage*, the kink band width is dictated by the distance between locations that experience the critical tensile strain for fiber breakage, which are determined based on fiber curvature. The evolution of curvature during the load history along the length of the mesoscale domain is demonstrated in Fig. 9. The material segment exhibits a slight gradient in curvature at lower loads, but localized peaks develop at two locations as the load increases. The

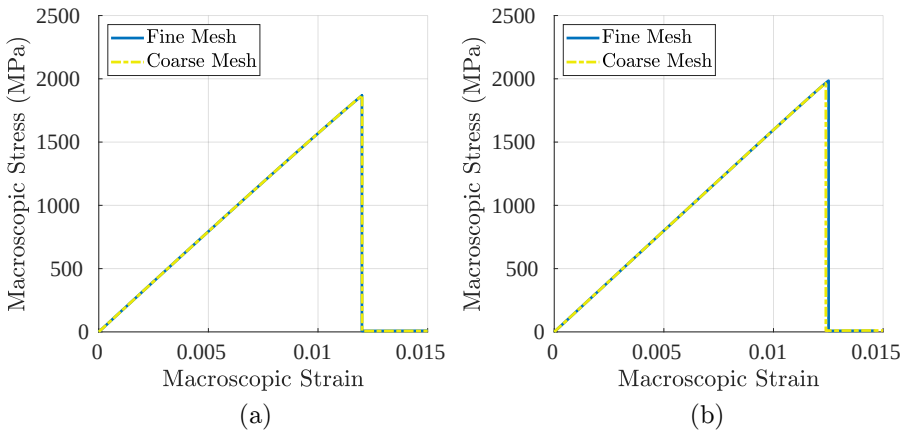


**Figure 8.** Sensitivity of the structural response to mesh size with the (a) local, and (b) nonlocal damage model formulations.

critical curvature is reached in the vicinity of the maximum load, the fibers break at peak curvature locations, and the kink band width stays constant thereafter. In the current study, the kink band width is defined as the distance between the element centroids that experience fiber breaks. Simultaneously, we observe the stress fields and matrix material behavior. The contour plots in Fig. 10a-b display the shear stress of the homogenized material and matrix damage state during the softening stage (macroscopic stress = $1959\,\mathrm{MPa}$). In the region of matrix softening, the in-plane shear stress, $\bar{\boldsymbol{\tau}}_{xz}$, has reached the strength of the homogenized material when loaded in simple shear (approximately $90\,\mathrm{MPa}$). The deformed and initial states of the highlighted elements near and inside the kink band are displayed in Fig. 10c, where the deformed elements are translated and clearly have lateral surface normals oriented at an angle compared to horizontal. In fact, periodicity causes the elements to have a form which resembles that of simple or pure shear state in the $xz$-plane. The greatest shear deformation is experienced in the element near mid-height with a ratio of shear to longitudinal strain: $\bar{\boldsymbol{\gamma}}_{xz}/\bar{\boldsymbol{\epsilon}}_{zz} \approx 1.92$. The outermost highlighted elements are also experiencing a shear-dominated deformation

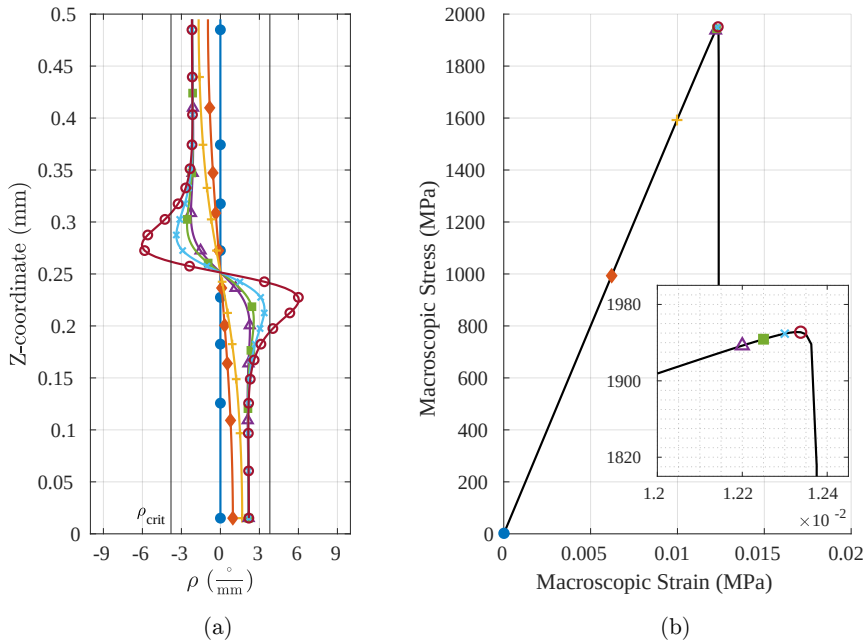


**Figure 9.** (a) Mesoscale curvature at select load levels. (b) Stress-strain response and select load levels. ($L_0 = 20\,\mu m$)

but the ratio of straining is smaller, $\bar{\gamma}_{xz}/\bar{\epsilon}_{zz} \approx 1.48$. The other normal and shear strain components are much smaller in all elements. Shear-dominated deformation in the kink band is consistent in all subsequent simulations and agrees with experimental observations like those of[24] where a softened external shear response signals the existence of a kink band. The value of the critical curvature is important since compressive strength is determined by the interplay between fiber breakage, matrix deformation and the buckling instability. As shown in Fig. 9, curvature peaks form prior to reaching the macroscopic strength, and quickly grow with localized deformation following the onset of buckling. If critical curvature occurs after the onset of buckling, matrix strength dictates the compressive strength of the composite. If critical curvature is reached prior to reaching the matrix deformation controlled buckling strength,

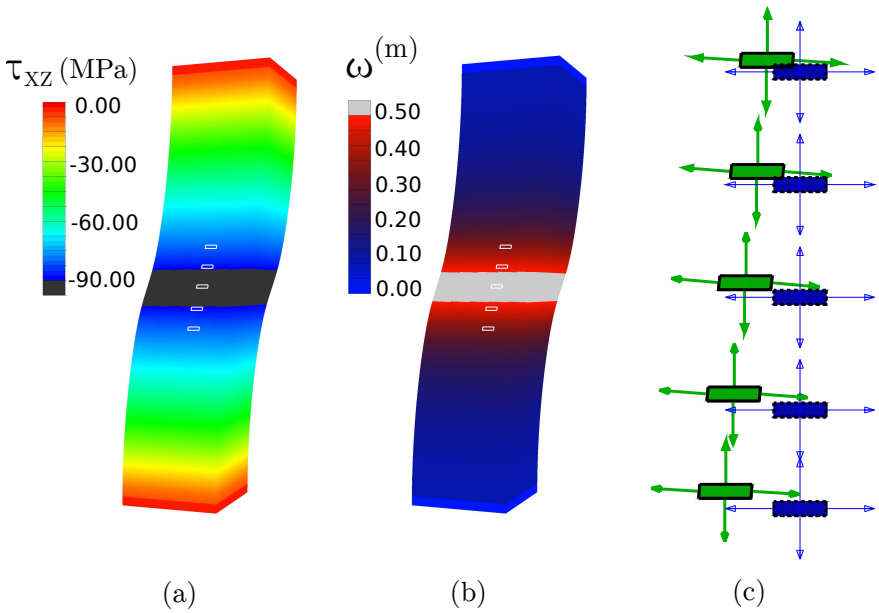


**Figure 10.** (a) Shear stress and (b) matrix damage during softening. (c) Parallel view of highlighted elements in deformed and initial state, including surface normal directions. ($L_0 = 20\,\mu\text{m}$, deformation 4x).

sudden fiber breakage determines the composite strength. As a first order approximation, we use a simple bending formula to compute $\rho_{\text{crit}} = 2\sigma^f_{\text{max}}/E^f d$ ($\sigma^f_{\text{max}} = 4.25\,\text{GPa}$ is the fiber tensile strength, $E^f = 280\,\text{GPa}$ is the fiber longitudinal modulus, $d = 8\,\mu\text{m}$ is the fiber diameter) that results in a fiber reaching its tensile strength at $3.8\ ^\circ/\text{mm}$. Using this criterion value, the relationship between the length scale parameter, $L_0$ and the resulting kink band width is shown in Fig. 11. The linear correlation already indicated in Eq. (16) is confirmed by the figure.

This linear relationship between the nonlocal length scale parameter and material properties allows us to control of the kink band width by adjusting the length scale parameter and using the linear relationship ($a = 1.21, b = 41.74$). The y-intercept in the figure indicates the predicted kink band width at the local limit, where the nonlocal model degenerates

to the local model. The relative insensitivity of the linear relationship to the constituent and composite parameters is shown in Fig. 12. The kink band width predictions for four composite materials using the length scale parameter selection via Eq. (16) are shown to agree with the results of the theoretical relationship Eq. (15) in Fig. 12.

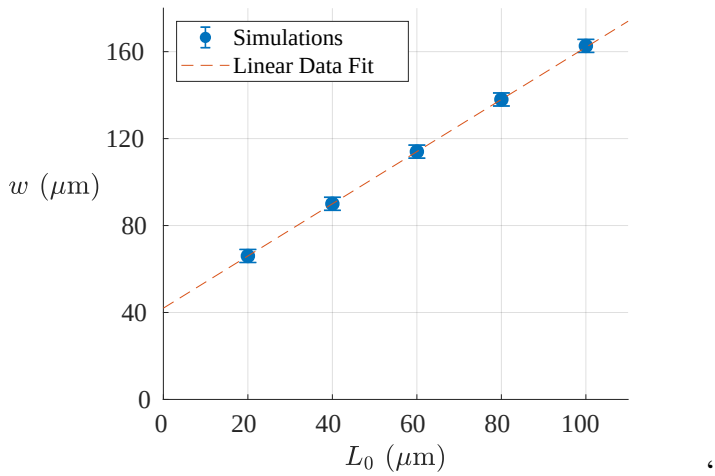


**Figure 11.** Relationship between nonlocal length scale parameter and kink band width.

*Misalignment Effects* The mesoscale investigations discussed thus far have included a misalignment form as expressed in Eqn. 25. With this waviness definition we are able to observe formation of a kink band. To account for uncertainty of the misalignment fields found in composites, the behavior of the model is investigated for variations of this damage localization feature. The effect of misalignment angle on strength is plotted in Fig. 13 for a range of misalignment angles corresponding to the magnitude of imperfections introduced during the composite specimen manufacturing process[45]. In the case of very small misalignment angle in the fibers, the response of the model is expected to be nearly elastic and consequently results in the highest strength prediction. The reduction in

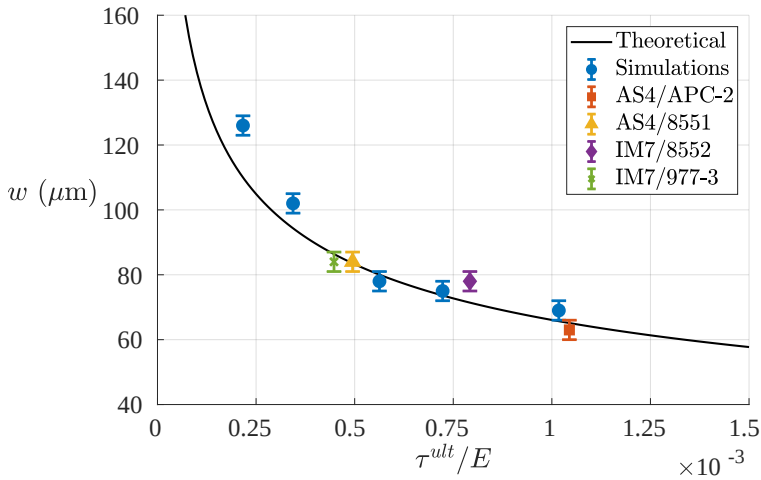


**Figure 12.** Kink band width predictions from simulations compared to analytical results, using calculated length scale value (material system properties referenced from [5,18,31,44]).

strength is attributed to the effect of the misalignment angle magnitude on instability initiation – a result that is consistent with the micromechanical analysis in [19]. We additionally compare our predictions to the relationship provided by [15], where the kinking stress is a function of the composite shear properties and misalignment angle alone. The multiscale model predicts a similar but shallower slope for low misalignment angles. The relationship between kink band failure strength and misalignment angle reinforces the notion of instability due to matrix material failure. Larger initial misalignment implies that the composite material is rotated compared to the external compression and more susceptible to undergoing shear-dominated deformation.

In addition to studying the effects of magnitude of misalignment angle with the sinusoidal fiber misalignment angle form we also explore how changing the shape of misalignment affects the compression strength. Initial fiber misalignment in the form of a Gaussian distribution is

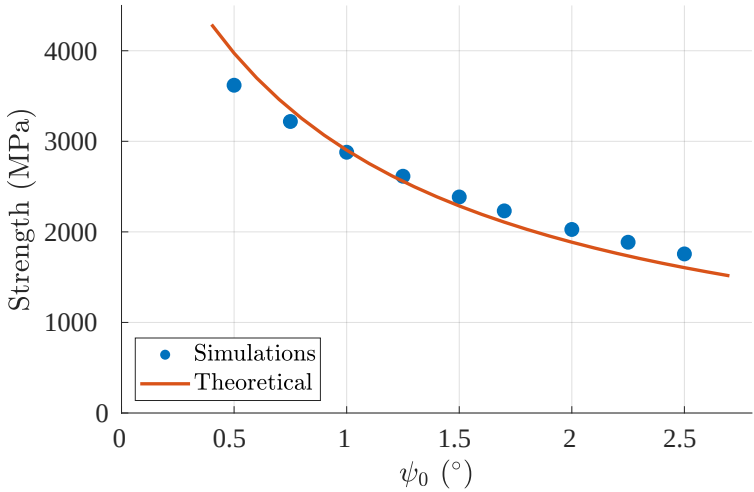


**Figure 13.** The effect of fiber misalignment angle on strength predictions, compared to [15].

also considered: $\mathcal{N}(\mu,\sigma) = \frac{1}{\sigma\sqrt{2\pi}}\exp\big(-\frac{1}{2}\big(\frac{z-\mu}{\sigma}\big)\big)$. The general forms of fiber misalignment investigated are illustrated in Fig. 14a. Decreasing the standard deviation value shrinks the region of initial maximum misalignment, and the effect of this misalignment localization on compression strength is shown in Figure 14b. There is a significant decrease in compression strength as the region of misalignment is localized (Fig. 14b reports strengths relative to the sinusoidal misalignment case). This conclusion is consistent with trends observed in direct numerical simulations [18]. Interestingly, the analysis of [24] considers a similar sinusoidal misalignment field and concludes that additional spatially localized imperfections have negligible effect on kink band width and failure strength. The somewhat gradually distributed fiber misalignment form described by a maximum misalignment angle used in this study has proved sufficient to initiate kink band formation within the bulk material and therefore model predictions can be taken as conservative.

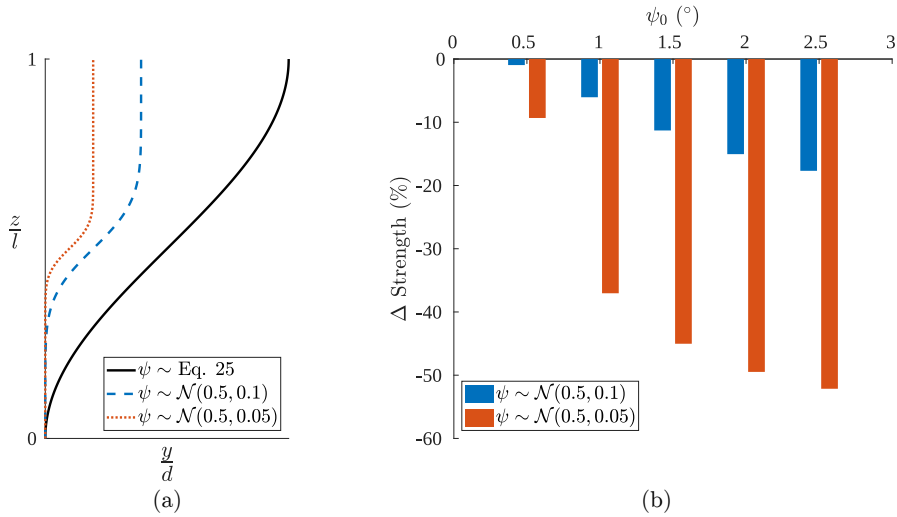


**Figure 14.** (a) Varied forms of initial fiber misalignment distribution. (b) Change in compression predictions with respect to sinusoidal fiber misalignment field.

*Shear nonlinearity effects* As presented in the model formulation section, the matrix material constituent of this EHM implementation has been modelled with degradeable properties according to an arctangent function for the damage potential. This material behavior neglects nonlinear shear effects that are found in plastic behavior of polymers, including cured epoxy resins. Examples of modified matrix behavior under shear are used in order to vary the nonlinearity of the microstructural model and are plotted in Fig. 15. As Fig. 15 shows, the initial shear modulus and ultimate strength values are constant in these cases, but the response shape through the ultimate strength varies from sharp (weak nonlinearity: $a^{(\mathrm{m})} = 190,\ b^{(\mathrm{m})} = 210$) to gradual (strong nonlinearity: $a^{(\mathrm{m})} = 0.58,\ b^{(\mathrm{m})} = 0.55$) softening and hardening behavior. The moderate case matches what has been used in the simulations presented thus far.

Simulations using the mesoscale problem setup are performed with all properties and parameters held constant while varying the shear

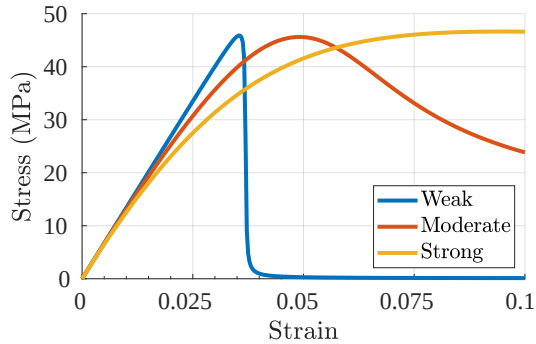


**Figure 15.** Example matrix shear behaviors ($L_0 = 31.7\,\mu\text{m}$)

nonlinearity behavior. The kink band results for the three cases are shown in Fig. 16. Since matrix damage of nearly $50\%$ causes the instability leading to kink band formation, the material state corresponding to that value was examined. The weak nonlinear matrix behavior leads to a fairly concentrated damage field prior to failure, wide bands of broken fibers, and $w \approx 51\,\mu\text{m}$. Conversely, applying strong shear nonlinearity results a broader damage field prior to kink band failure, concentrated locations of fiber break, and $w \approx 126\,\mu\text{m}$; recall that the moderate nonlinearity results in $w \approx 80\,\mu\text{m}$. In the strong nonlinearity case there are larger strains at locations further from the maximum initial misalignment, and the material in this relatively wide region rotates to be subject to shear-dominant strain under the compressive load. The trend of these results align with observations of composites with more ductile thermoplastic materials, which exhibit larger kink band widths (approximately 20 times the fiber diamater)[5,10] compared to more brittle toughened epoxy matrix materials (approximately 10 times the fiber diameter)[18,44]. Several experiments have been conducted on UD carbon fiber/epoxy composite configurations which produce high quality in situ and post mortem images of kink band morphology at the microscopic scale. The kink band forms displayed in

Fig. 16 agree with experimental results in in Wang et al.[7] and Sun et al.[9] from composites containing standard modulus carbon fibers, and Gutkin et al.[8] from a composite containing intermediate modulus carbon fibers. The composite properties considered in this investigation most closely match those of Gutkin et al.[8], and the kink band width is shown to be less than $100\,\mu\mathrm{m}$. The test procedures, equipment, and materials in these experiments are all different but fall under the category of UD carbon fiber/epoxy specimens under longitudinal compression. Briefly described, these are conducted with (a) a (standard) Combined Loading Compression (CLC) test fixture and single edge notched (SEN) plates[9]; (b) a Scanning Electron Microscopy (SEM) screw-driven test jig and SEN plates[8]; (c) uniaxial compression on waisted rods[7].

## Conclusions

In this manuscript, we presented a multiscale model to predict the progression of damage in a fibrous composite under compression. Kink band formation is predicted with a nonlocal damage gradient regularization scheme coupled to a computational homogenization method in solving the macrostructural response. We are able to employ quasi-static analyses to investigate the instability-driven kink band failure mechanism. The kink band initiates due to matrix softening that results in the onset of buckling and is completely formed when fibers break as a result of localized curvature. Overall, the predicted effects of material properties and fiber misalignment angle on kink band width and failure strength corroborate analytical and experimental results in the literature. The effects of nonlinear shear behavior of the matrix material were also shown to contribute significantly to the kink band width and should be taken into account when calibrating the model to a specific matrix constituent material. Additional features of the presented multiscale approach are: (1) the homogenized model is able to capture

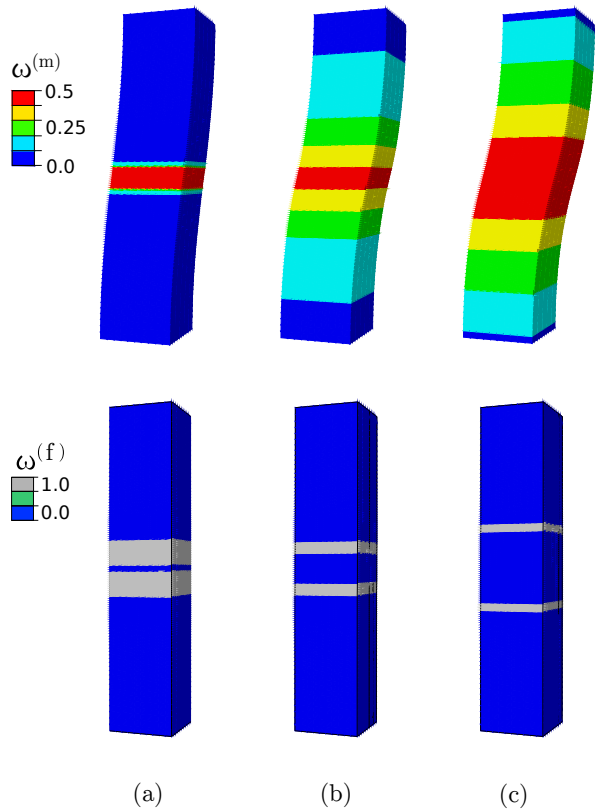


**Figure 16.** Matrix damage at kink band initiation, and fiber break fields corresponding to (a) weak, (b) moderate, and (c) strong nonlinear shear matrix response.

various kink band widths without geometric representation of the fibers; and (2) only a small amount of mesh sensitivity is observed and the model also exhibits convergent predictions with an implicit FE analysis procedure, thereby allowing application of the model for simulation of experimental configurations. The proposed model holds the potential to be used in analysis of larger scale laminated structures as well. The multiscale approach allows discernment and efficiency in exploring the aspects that make up the kink band problem.

### Future Work

The kink band problem is not unique to the unidirectional, or prepreg tape, composite with CFRP material properties investigated here. Future work to facilitate design of materials could include validating the model against different material systems. Experimental results of a unidirectionally reinforced metal matrix composites (MMC) also present kink band failure (see e.g.,[46]) and the authors are not aware of mesoscale investigations with MMC material properties. Additionally, the proposed methodology is applicable to other long fiber reinforced composites including 2D/3D fiber preform reinforced composites where kink band failure occurs (see e.g.,[47]) by appropriately defining the local fiber orientation in the part. Woven preforms can also be investigated by the proposed approach, but that requires a change in the microstructure and the associated reduced order model.

## Acknowledgements

The authors gratefully acknowledge the financial support of the Air Force Research Laboratory (through Contract No: FA8650-12-D-3212/0016 under University of Dayton Research Institute Subcontract No. RSC16122 as well as Air Force Research Laboratory SIRCA Award No: FA8650-19-2-2214). The authors also acknowledge the support of the USA-Israel Air Vehicle Technologies Project Agreement (AVT PA).

## References

1. Stephen B Clay and Philip M Knoth. Experimental results of quasi-static testing for calibration and validation of composite progressive damage analysis methods. *Journal of Composite Materials*, 51(10):1333–1353, 2017. DOI:10.1177/0021998316658539. URL https://doi.org/10.1177/0021998316658539.
2. Lucas L Vignoli, Marcelo A Savi, Pedro MCL Pacheco, and Alexander L Kalamkarov. Micromechanical analysis of longitudinal and shear strength of composite laminae. *Journal of Composite Materials*, 54(30):4853–4873, 2020. DOI:10.1177/0021998320936343. URL https://doi.org/10.1177/0021998320936343.

3. Soutis C, Curtis PT and Fleck NA. Compressive failure of notched carbon fibre composites. *Proceedings: Mathematical and Physical Sciences* 1993; 440(1909): 241–256. URL http://www.jstor.org/stable/52233.
4. Kyriakides S, Arseculeratne R, Perry E et al. On the compressive failure of fiber reinforced composites. *International Journal of Solids and Structures* 1995; 32(6): 689 – 738. DOI: https://doi.org/10.1016/0020-7683(94)00157-R. URL http://www.sciencedirect.com/science/article/pii/002076839400157R. Time Dependent Problems in Mechanics.
5. Vogler T and Kyriakides S. Initiation and axial propagation of kink bands in fiber composites. *Acta Materialia* 1997; 45(6): 2443 – 2454. DOI:https://doi.org/10.1016/S1359-6454(96)00350-3. URL http://www.sciencedirect.com/science/article/pii/S1359645496003503.
6. Schapery R. Prediction of compressive strength and kink bands in composites using a work potential. *International Journal of Solids and Structures* 1995; 32(6): 739 – 765. DOI: https://doi.org/10.1016/0020-7683(94)00158-S. URL http://www.sciencedirect.com/science/article/pii/002076839400158S. Time Dependent Problems in Mechanics.
7. Wang Y, Burnett TL, Chai Y et al. X-ray computed tomography study of kink bands in unidirectional composites. *Composite Structures* 2017; 160: 917 – 924. DOI:https://doi.org/10.1016/j.compstruct.2016.10.124. URL http://www.sciencedirect.com/science/article/pii/S0263822316317159.
8. R. Gutkin, S.T. Pinho, P. Robinson, and P.T. Curtis. On the transition from shear-driven fibre compressive failure to fibre kinking in notched cfrp laminates under longitudinal compression. *Composites Science and Technology*, 70(8):1223–1231, 2010. ISSN 0266-3538. DOI:https://doi.org/10.1016/j.compscitech.2010.03.010. URL https://www.sciencedirect.com/science/article/pii/S0266353810001119.
9. Sun Q, Guo H, Zhou G et al. Experimental and computational analysis of failure mechanisms in unidirectional carbon fiber reinforced polymer laminates under longitudinal compression loading. *Composite Structures* 2018; 203: 335–348. DOI:https://doi.org/10.1016/j.compstruct.2018.06.028. URL https://www.sciencedirect.com/science/article/pii/S0263822318313278.
10. Moran P, Liu X and Shih C. Kink band formation and band broadening in fiber composites under compressive loading. *Acta Metallurgica et Materialia* 1995; 43(8): 2943 – 2958. DOI: https://doi.org/10.1016/0956-7151(95)00001-C. URL http://www.sciencedirect.com/science/article/pii/095671519500001C.

11. Moran P and Shih C. Kink band propagation and broadening in ductile matrix fiber composites: Experiments and analysis. *International journal of solids and structures* 1998; 35(15): 1709–1722.
12. *Mechanics of composite strengthening.*, 1965. URL https://ntrs.nasa.gov/search.jsp?R=19660035520.
13. Argon AS. Fracture of Composites. *Treatise on Materials Science and Technology* 1972; 1: 79–114.
14. Budiansky B. Micromechanics. *Computers & Structures* 1983; 16(1): 3 – 12. DOI: https://doi.org/10.1016/0045-7949(83)90141-4. URL http://www.sciencedirect.com/science/article/pii/0045794983901414.
15. Budiansky B and Fleck N. Compressive failure of fibre composites. *Journal of the Mechanics and Physics of Solids* 1993; 41(1): 183,211.
16. Fleck NA, Deng L and Budiansky B. Prediction of Kink Width in Compressed Fiber Composites. *Journal of Applied Mechanics* 1995; 62(2): 329–337. DOI: 10.1115/1.2895935. URL https://doi.org/10.1115/1.2895935. https://asmedigitalcollection.asme.org/appliedmechanics/article-pdf/62/2/329/4737376/329_1.pdf.
17. Yerramalli C and Waas A. The effect of fiber diameter on the compressive strength of composites - a 3d finite element based study. *Computer Modeling in Engineering and Sciences* 2004; 6: 1–16.
18. Bishara M, Rolfes R and Allix O. Revealing complex aspects of compressive failure of polymer composites – part i: Fiber kinking at microscale. *Composite Structures* 2017; 169: 105 – 115. DOI:https://doi.org/10.1016/j.compstruct.2016.10.092. URL http://www.sciencedirect.com/science/article/pii/S026382231632222X. In Honor of Prof. Leissa.
19. F. Naya, M. Herráez, C.S. Lopes, C. González, S. Van der Veen, and F. Pons. Computational micromechanics of fiber kinking in unidirectional frp under different environmental conditions. *Composites Science and Technology*, 144:26 – 35, 2017. ISSN 0266-3538. DOI:https://doi.org/10.1016/j.compscitech.2017.03.014. URL http://www.sciencedirect.com/science/article/pii/S0266353817300416.
20. Bergan AC, Herráez M, González C et al. A constitutive model for fiber kinking: Formulation, finite element implementation, and verification. *Composites Part A: Applied Science and Manufacturing* 2020; 129: 105682. DOI:https://doi.org/10.1016/j.compositesa.2019.105682. URL https://www.sciencedirect.com/science/article/pii/S1359835X19304312.

21. Pinho S, Darvizeh R, Robinson P et al. Material and structural response of polymer-matrix fibre-reinforced composites. *Journal of Composite Materials* 2012; 46(19-20): 2313–2341. DOI:10.1177/0021998312454478. URL https://doi.org/10.1177/0021998312454478. https://doi.org/10.1177/0021998312454478.
22. Camanho P, Arteiro A, Melro A et al. Three-dimensional invariant-based failure criteria for fibre-reinforced composites. *International Journal of Solids and Structures* 2015; 55: 92–107. DOI:https://doi.org/10.1016/j.ijsolstr.2014.03.038. URL https://www.sciencedirect.com/science/article/pii/S0020768314001449. Special Issue Computational and Experimental Mechanics of Advanced Materials A workshop held at King Abdullah University of Science and Technology Jeddah, Kingdom of Saudi Arabia July 1-3, 2013.
23. Wilhelmsson D, Talreja R, Gutkin R et al. Compressive strength assessment of fibre composites based on a defect severity model. *Composites Science and Technology* 2019; 181: 107685. DOI:https://doi.org/10.1016/j.compscitech.2019.107685. URL https://www.sciencedirect.com/science/article/pii/S0266353819303483.
24. Vogler T, Hsu SY and Kyriakides S. On the initiation and growth of kink bands in fiber composites. part ii: analysis. *International Journal of Solids and Structures* 2001; 38(15): 2653,2682.
25. Liu D, Fleck N and Sutcliffe M. Compressive strength of fibre composites with random fibre waviness. *Journal of the Mechanics and Physics of Solids* 2004; 52(7): 1481 – 1505. DOI: https://doi.org/10.1016/j.jmps.2004.01.005. URL http://www.sciencedirect.com/science/article/pii/S0022509604000110.
26. Fish J and Shek K. Multiscale analysis of composite materials and structures. *Composites Science and Technology* 2000; 60(12): 2547–2556. DOI:https://doi.org/10.1016/S0266-3538(00)00048-8. URL https://www.sciencedirect.com/science/article/pii/S0266353800000488.
27. Crouch R and Oskay C. Symmetric mesomechanical model for failure analysis of heterogeneous materials. *International Journal for Multiscale Computational Engineering* 2010; 8(5): 447–461.
28. Oskay C and Fish J. Eigendeformation-based reduced order homogenization for failure analysis of heterogeneous materials. *Computer Methods in Applied Mechanics and Engineering* 2007; 196: 1216–1243.
29. Sparks P and Oskay C. The method of failure paths for reduced-order computational homogenization. *International Journal for Multiscale Computational Engineering* 2016; 14(5): 515–534.

30. Zhang X and Oskay C. Eigenstrain based reduced order homogenization for polycrystalline materials. *Computer Methods in Applied Mechanics and Engineering* 2015; 297: 408 – 436. DOI:https://doi.org/10.1016/j.cma.2015.09.006. URL http://www.sciencedirect.com/science/article/pii/S004578251500300X.
31. Bogdanor MJ and Oskay C. Prediction of progressive damage and strength of im7/977-3 composites using the eigendeformation-based homogenization approach: Static loading. *Journal of Composite Materials* 2017; 51(10): 1455–1472. DOI:10.1177/0021998316650982. URL https://doi.org/10.1177/0021998316650982. https://doi.org/10.1177/0021998316650982.
32. Oskay C. Two-level multiscale enrichment methodology for modeling of heterogeneous plates. *International Journal for Numerical Methods in Engineering* 2009; 80(9): 1143–1170. DOI:https://doi.org/10.1002/nme.2652. URL https://onlinelibrary.wiley.com/doi/abs/10.1002/nme.2652. https://onlinelibrary.wiley.com/doi/pdf/10.1002/nme.2652.
33. Yan H, Oskay C, Krishnan A et al. Compression-after-impact response of woven fiber-reinforced composites. *Composites Science and Technology* 2010; 70(14): 2128 – 2136. DOI:https://doi.org/10.1016/j.compscitech.2010.08.012. URL http://www.sciencedirect.com/science/article/pii/S0266353810003209.
34. Bensoussan A. *Asymptotic analysis for periodic structures / Alain Bensoussan, Jacques-Louis Lions, George Papanicolaou.* Studies in mathematics and its applications ; 5, Amsterdam ;: North-Holland Pub. Co., 1978. ISBN 0444851720.
35. Guedes J and Kikuchi N. Preprocessing and postprocessing for materials based on the homogenization method with adaptive finite element methods. *Computer Methods in Applied Mechanics and Engineering* 1990; 83(2): 143–198. DOI:https://doi.org/10.1016/0045-7825(90)90148-F. URL https://www.sciencedirect.com/science/article/pii/004578259090148F.
36. Dvorak GJ and Benveniste Y. On transformation strains and uniform fields in multiphase elastic media. *Proceedings of the Royal Society of London Series A: Mathematical and Physical Sciences* 1992; 437(1900): 291–310. DOI:10.1098/rspa.1992.0062. URL https://royalsocietypublishing.org/doi/abs/10.1098/rspa.1992.0062. https://royalsocietypublishing.org/doi/pdf/10.1098/rspa.1992.0062.
37. Oskay C, Su Z and Kapusuzoglu B. Discrete eigenseparation-based reduced order homogenization method for failure modeling of composite materials. *Computer Methods in Applied Mechanics and Engineering* 2020; 359: 112656. DOI:https://doi.org/10.1016/j.cma.

2019.112656. URL http://www.sciencedirect.com/science/article/pii/S0045782519305419.

38. Bacigalupo A and Gambarotta L. Second-order computational homogenization of heterogeneous materials with periodic microstructure. *ZAMM - Journal of Applied Mathematics and Mechanics / Zeitschrift für Angewandte Mathematik und Mechanik* 2010; 90(10-11): 796–811. DOI:https://doi.org/10.1002/zamm.201000031. URL https://onlinelibrary.wiley.com/doi/abs/10.1002/zamm.201000031. https://onlinelibrary.wiley.com/doi/pdf/10.1002/zamm.201000031.
39. Idiart M, Moulinec H, Ponte Castañeda P et al. Macroscopic behavior and field fluctuations in viscoplastic composites: Second-order estimates versus full-field simulations. *Journal of the Mechanics and Physics of Solids* 2006; 54(5): 1029–1063. DOI:https://doi.org/10.1016/j.jmps.2005.11.004. URL https://www.sciencedirect.com/science/article/pii/S0022509605002188.
40. Poh LH and Sun G. Localizing gradient damage model with decreasing interactions. *International Journal for Numerical Methods in Engineering* 2017; 110(6): 503–522.
41. Seupel A, Hütter G and Kuna M. An efficient fe-implementation of implicit gradient-enhanced damage models to simulate ductile failure. *Engineering Fracture Mechanics* 2018; 199: 41 – 60. DOI:https://doi.org/10.1016/j.engfracmech.2018.01.022. URL http://www.sciencedirect.com/science/article/pii/S0013794417311669.
42. Nolan D, Lally C and McGarry J. Understanding the deformation gradient in abaqus and key guidelines for anisotropic hyperelastic user material subroutines (umats). *Journal of the Mechanical Behavior of Biomedical Materials* 2022; 126: 104940. DOI:https://doi.org/10.1016/j.jmbbm.2021.104940. URL https://www.sciencedirect.com/science/article/pii/S1751616121005713.
43. Robotic systems, chapter 4. 3d rotations, 2020. URL http://motion.cs.illinois.edu/RoboticSystems/.
44. Lee J and Soutis C. A study on the compressive strength of thick carbon fibre–epoxy laminates. *Composites Science and Technology* 2007; 67(10): 2015–2026. DOI:https://doi.org/10.1016/j.compscitech.2006.12.001. URL https://www.sciencedirect.com/science/article/pii/S0266353806004520.
45. Sutcliffe M, Lemanski S and Scott A. Measurement of fibre waviness in industrial composite components. *Composites Science and Technology* 2012; 72(16): 2016 – 2023. DOI:https://doi.org/10.1016/j.compscitech.2012.09.001. URL http://www.sciencedirect.com/science/article/pii/S0266353812003235.

825 46. H Zhang, K Cho, C. F Yen, and K Ravi-Chandar. Dynamic crushing of unidirectionally
826 reinforced metal matrix composite. *Strain*, 50(6):517–526, 2014. ISSN 0039-2103. DOI:
827 https://doi.org/10.1111/str.12103.
828 47. Roberts Joffe, David Mattsson, Janis Modniks, and Janis Varna. Compressive
829 failure analysis of non-crimp fabric composites with large out-of-plane misalignment
830 of fiber bundles. *Composites Part A: Applied Science and Manufacturing*, 36(8):
831 1030–1046, 2005. ISSN 1359-835X. DOI:https://doi.org/10.1016/j.compositesa.2004.
832 10.028. URL `https://www.sciencedirect.com/science/article/pii/`
833 `S1359835X04002726`. ACMC/SAMPE Conference on Marine Composites (MarComp)
834 2003.